Supplementary Material

High-valent W doped CeO_2 regulates Cu-Cd-SSZ-13 for enhancing NH_3-SCR performance

Min Li[a], Chong Chen[a], Weijuan Chen[a], Yuan Pan*[a] Yunqi Liu*[a,b]

[a]State Key Laboratory of Heavy Oil Processing, China University of Petroleum (East China), Qingdao 266580, China

[b]School of Chemistry and Materials Science, Anhui Normal University, Wuhu 241002, China

*Corresponding Author. E-mail: panyuan@upc.edu.cn (Y. Pan), liuyq@upc.edu.cn (Y. Liu)

1. Experimental details

Materials

$Cu(CH_3COO)_2 \cdot H_2O$ (99% AR grade), $Ce(NO_3)_3 \cdot 6H_2O$ (99% AR grade), $(NH_4)10W_{12}O_{41} \cdot xH_2O$ (99% AR grade), $(C_6H_9NO)_n$ were purchased from Aladdin Industrial Corporation, SSZ-13 (Si/Al=8) with H^+ was purchased from Anhui Na Lan environmental protection Technology Co. LTD. The deionized water was used for all experiments.

Characterization

X-ray diffraction (XRD) patterns were recorded on an X'Pert PRO MPD diffractometer (Malvern Panalytical, Netherlands) using Cu Kα radiation (λ = 1.5406 Å) operating at 40 kV and 40 mA. The patterns were collected in the 2θ range of 5–75° with a step size of 0.02° and a scan rate of $5° \cdot min^{-1}$. The morphology of the catalysts was observed by scanning electron microscopy (SEM, S-4800, Hitachi High-Technologies Corporation, Japan) and transmission electron microscopy (TEM, JEM-2100, JEOL Ltd., Japan). For SEM analysis, the catalyst powder was dispersed on a conductive carbon tape and sputter-coated with gold to enhance conductivity. For TEM analysis, the sample was ultrasonically dispersed in ethanol, dropped onto a copper grid with a carbon film, and dried at room temperature prior to observation. The elemental composition of the catalysts was determined by inductively coupled plasma atomic emission spectroscopy (ICP-AES, Agilent 720, Agilent Technologies, USA). Prior to analysis, approximately 20 mg of the catalyst sample was dissolved in a acid solution using a microwave digestion system. The resulting solution was diluted to a suitable concentration with deionized water before measurement. The N_2 adsorption-desorption isotherms were measured at -196 °C (77 K) using a ChemBET 3000 sorption apparatus (Quantachrome Instruments, USA). Prior to measurement, each sample (ca. 100 mg) was degassed under vacuum (< 10^{-2} Pa) at 350 °C for 4 h to remove adsorbed impurities. The specific surface area was calculated using the Brunauer–Emmett–Teller (BET) method, and the total pore volume was obtained from the amount adsorbed at a relative pressure (P/P_0) of approximately 0.99. UV–vis DRS spectra were obtained in the range of 200–800 nm on a λ Lambda 950 spectrometer (PerkinElmer, Massachusetts, USA). The X-ray photoelectron spectroscopy (XPS) measurements were performed on an ESCALAB MK II electron spectrometer (Thermo Fisher Scientific, UK) using monochromatic

Al Kα radiation (hν = 1486.6 eV) operating at 150 W. Electron paramagnetic resonance (EPR) spectra were recorded on an EMPplus-10/12 spectrometer (Bruker Corporation, Germany) at X-band (9.4 GHz) at room temperature and at -196 °C (77 K). The microwave power was set to 10 mW, and the modulation frequency was 100 kHz. Prior to measurement, the catalyst sample was transferred to a quartz EPR tube and sealed under ambient conditions without further pretreatment to preserve the oxygen vacancy state. The XAFS spectra were obtained in B L14W1/BL11B station of SSRF (Shanghai Synchrotron Radiation Facility, China).

To analyze the coordination state and structural integrity of Al species in the catalyst before and after hydrothermal aging, the ^{27}Al magic-angle spinning nuclear magnetic resonance (^{27}Al MAS NMR) spectra were recorded on an Avance III HD 400 MHz spectrometer (Bruker Corporation, USA) at a magnetic field strength of 11.7 T. The resonance frequency for ^{27}Al was 104.3 MHz. The samples were packed into 4 mm ZrO_2 rotors and spun at a rate of 12 kHz. A single-pulse sequence with a pulse width of 0.5 μs and a recycle delay of 1 s was employed. The chemical shifts were referenced to a 1 M $Al(NO_3)_3$ solution at 0 ppm. Prior to measurement, the catalysts were dried under vacuum at 120 °C for 12 h to remove adsorbed water. Subsequently, the samples were transferred into a quartz tube and heated to 550 °C at a rate of 5 °C/min under flowing high-purity N_2 (or He) atmosphere and held for 4 h to remove the template, adsorbed CO_2, and other organic impurities. The samples were cooled naturally to room temperature under N_2 or He atmosphere, then the samples quickly loaded into a 4 mm ZrO_2 rotor and compacted to ensure good thermal conductivity and radiofrequency matching. Temperature programmed reduction by H_2 (H_2-TPR) was measured with a Micromeritics AutoChem 2950 HP instrument (Micromeritics Instrument Corporation, USA) with a thermal conductivity detector (TCD) detector. An amount of 100 mg of each sample was used for each measurement. Before the introduction of the sample to the H_2-Ar stream, the sample was pretreated in a He stream at 350 °C for 30 min. H_2-TPR started from 80 °C to 800 °C at a rate of 10 °C·min^{-1}.The temperature-programmed desorption of ammonia (NH_3-TPD) experiments were performed using a Micromeritics AutoChemII 2950 HP instrument (Micromeritics Instrument Corporation, USA) with TCD under helium flow. An amount of 100 mg of each sample was pretreated in He flowing at 350 °C for 1 h. Then, each sample was saturated with

10% NH_3/N_2 at 70°C for 1 h, followed by being flushed by He at 80 °C for 1 h. Subsequently, the sample was heated to 700 °C in He flowing at a rate of 10 °C·min^{-1}.

The Pyridine Infrared Spectroscopy (Py-IR) spectra were recorded on the FTIR spectrometer (Nicolet iS50, Thermo Fisher Scientific, USA). The catalyst powder to be tested was thoroughly ground, and approximately 10-20 mg of the ground sample was pressed into a self-supporting wafer. The resulting wafer was fixed in a quartz infrared sample cell which was equipped with CaF_2 windows. Prior to pyridine adsorption, the sample was subjected to high-temperature vacuum activation. The temperature was raised to 450 °C at a ramp rate of 5 °C min^{-1}, maintained at this temperature for 4 h, and then cooled to 50 °C. During the adsorption step, pyridine was evaporated at room temperature and introduced into the sample cell under vacuum. Adsorption was carried out under saturated vapor pressure. To ensure thorough contact between pyridine and the acid sites, the sample was held at the adsorption temperature for 15 min. Subsequently, the temperature was sequentially raised to 150, 250, and 350 °C for spectroscopic measurements. After the adsorption step, the sample cell was evacuated at the same temperature (50 °C) to remove physisorbed pyridine. *In situ* diffuse reflectance infrared Fourier transform spectroscopy (*in situ* DRIFTS) was performed on a VERTEX 70 FTIR spectrometer (Bruker Corporation, Germany) equipped with a Harrick Scientific DRIFT cell and a liquid nitrogen-cooled MCT detector. All spectra were recorded in the range of 4000–1000 cm^{-1} with a resolution of 4 cm^{-1} and 64 scans per spectrum, presented in Kubelka–Munk format. Prior to each experiment, the catalyst powder was pretreated *in situ* at 350 °C in N_2 flow (30 mL min^{-1}) for 30 min to remove adsorbed species. The background spectrum was collected under the same conditions and automatically subtracted from the sample spectra. For adsorption experiments, the gas flow was switched to 500 ppm NH_3/N_2 or 500 ppm NO/N_2 at a total flow rate of 50 mL min^{-1}, and spectra were recorded at various temperatures from 50 °C to 350 °C. For transient reaction experiments, the gas composition was switched between NH_3 and NO + O_2 to monitor the formation and consumption of surface species.

Catalytic Activity Test

The composition of the reaction gas as follows: 500 ppm NH_3, 500 ppm NO, 5 % O_2, N_2 as balance gas, 50 ppm SO_2 (when used), and 5 vol% H_2O (when used). The composition and

concentration of the outlet gas was analyzed by flue gas analyzer (MRU OPTIMA 7). The reaction temperature in the range of 100−550 °C, the total gas flow rate was 450 mL/min, and the GHSV from 60000 to 300000 h^{-1}. The hydrothermal process at 800 ℃ for 48 h.

During hydrothermal aging process, high-purity N_2 was used as the carrier gas, and water vapor was introduced by bubbling method. First, N_2 (300 mL·min^{-1}) was introduced to expel the air in the device for 30 minutes. Then, the temperature was increased at a rate of 5 °C·min^{-1} to the target hydrothermal aging temperature (800 °C) and hydrothermal-aging for 12 h. After the hydrothermal aging process was completed, the water vapor generator was turned off, and the carrier gas was maintained flowing while the temperature was decreased at a rate of 5 ℃·min^{-1} to room temperature. The hydrothermal aging catalyst was collected in a desiccator and sealed for storage, which was used for the NH_3-SCR performance test.

The NO conversion, NO oxidation conversion, and N_2 selectivity were calculated by the following equation:

$$\text{NO conversion} = \frac{[NO]_{in} - [NO]_{out}}{[NO]_{in}} \times 100\% \quad (1)$$

$$\text{NO oxidation conversion} = \frac{[NO]_{in} - [NO]_{out}}{[NO]_{in}} \times 100\% \quad (2)$$

$$N_2 \text{ selectivity} = \left(1 - \frac{2[N_2O]_{out}}{[NO_x]_{in} + [NH_3]_{in} - [NO_x]_{out} - [NH_3]_{out}}\right) \times 100\% \quad (3)$$

Assuming the reaction atmosphere is not limited by diffusion, the SCR reaction rate and Turnover frequency (TOF) can be calculated by the following formula after the mass and specific surface area of the catalyst are normalized:

$$\text{rate} = \frac{X_{NO} \times Q \times C_f}{V_m \times W \times S_{BET}} \quad (4)$$

$$TOF = \frac{Q \times X_{NO} \times 63.5[\frac{g}{mol}]}{V_m \times W \times M_{Cu^{2+}}[\%]} \quad (5)$$

where X_{NO} is the NO reduction conversion, Q is the volumetric flow rate (7.5×10^{-3} L/s), C_f is the concentration of NO (500 ppm), V_m is the molar volume of gas (22.4 L/mol), W is the

catalyst weight (g) and S_{BET} is the specific area of the catalyst (m^2/g), M_{Cu2+} is mass fraction of isolated Cu^{2+}.

2. Supplementary Figures S1–S24

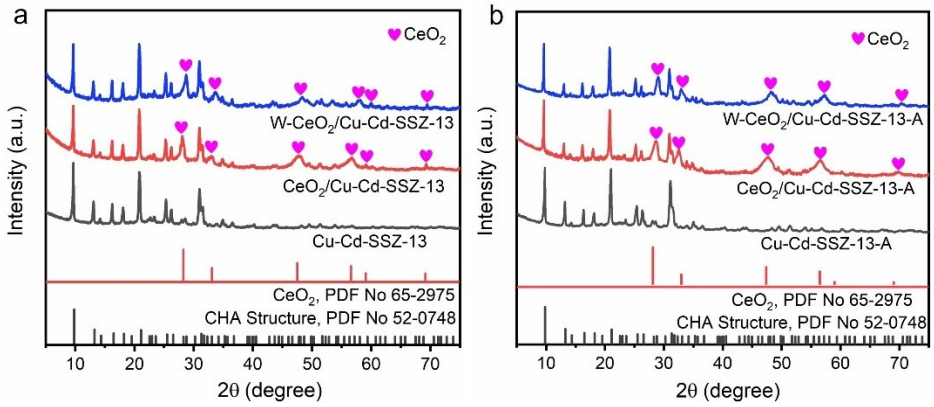

Fig. S1 XRD pattern of catalysts (a) before, (b) after hydrothermal ageing.

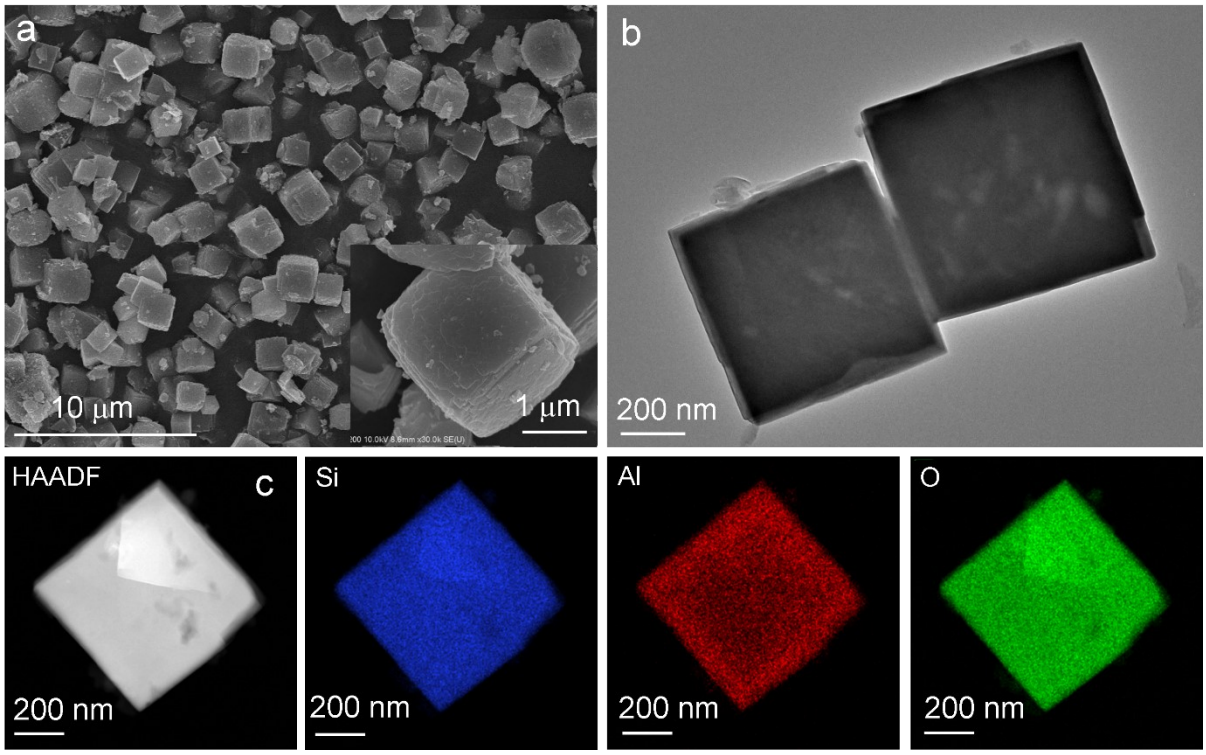

Fig. S2 (a) SEM, (b) TEM and (c) HAADF-STEM and EDS mapping images of parent SSZ-13.

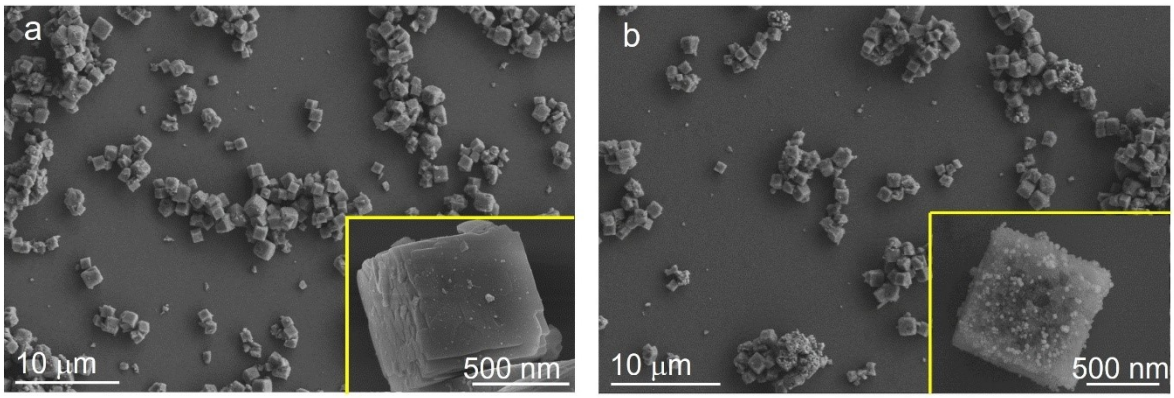

Fig. S3 SEM images of (a) Cu-Cd-SSZ-13 and (b) CeO_2/Cu-Cd-SSZ-13.

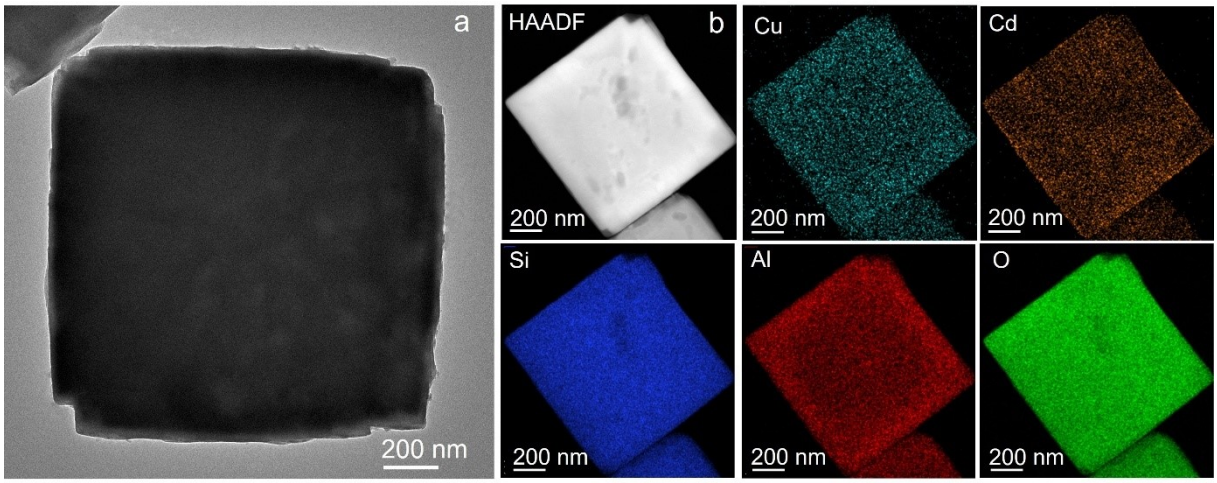

Fig. S4 (a) HRTEM and (b) HAADF-STEM and EDS mapping images of Cu-Cd-SSZ-13.

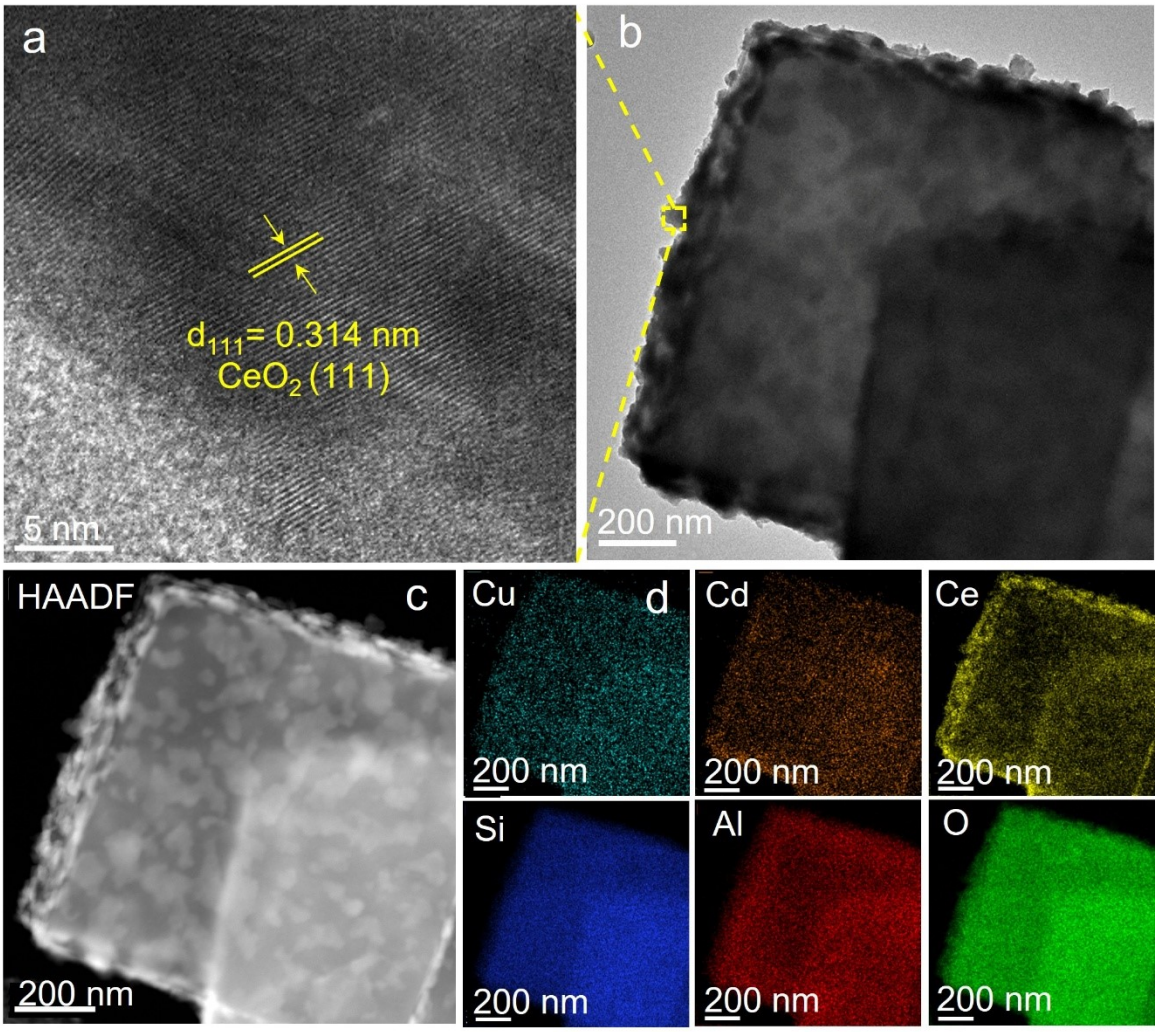

Fig. S5 (a, b) HRTEM and (c, d) HAADF-STEM and EDS images of CeO_2/Cu-Cd-SSZ-13.

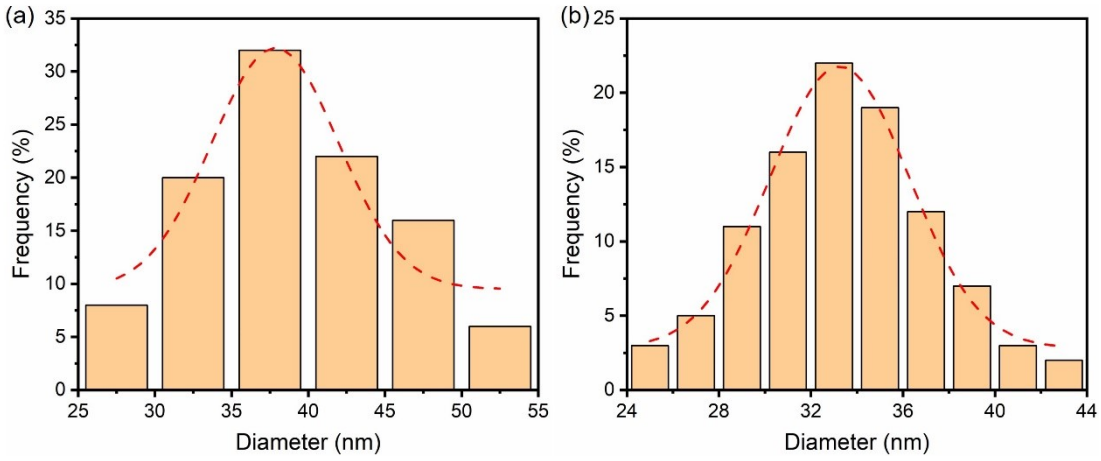

Fig. S6 The diameter of CeO_2 particles in (a) CeO_2/Cu-Cd-SSZ-13 and (b) W-CeO_2/Cu-Cd-SSZ-13.

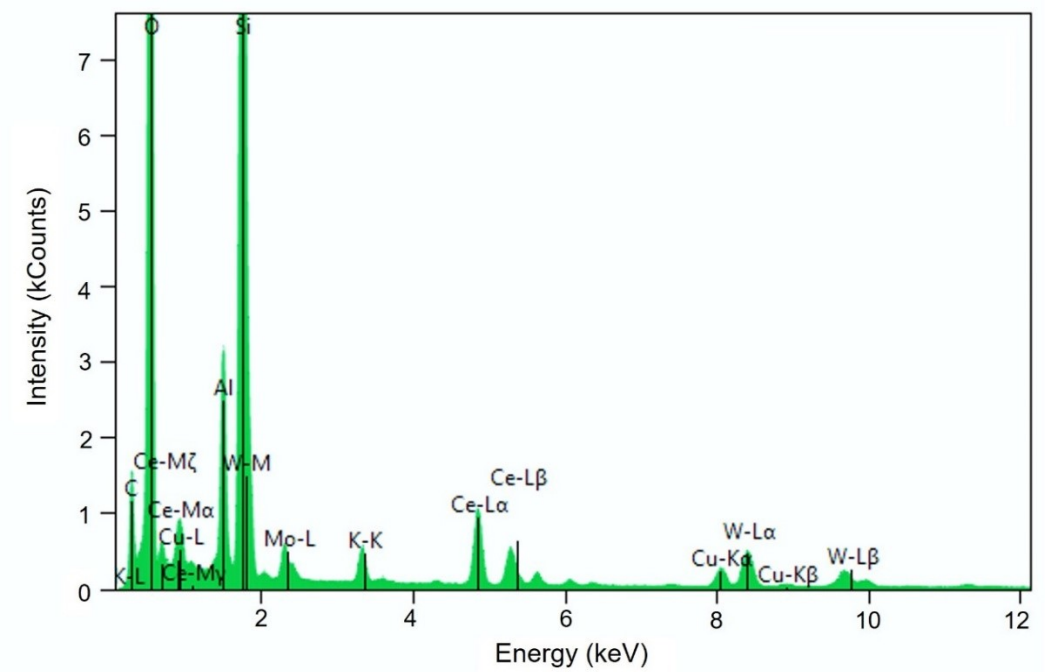

Fig. S7. The EDS image of the selected area in Fig. 1d.

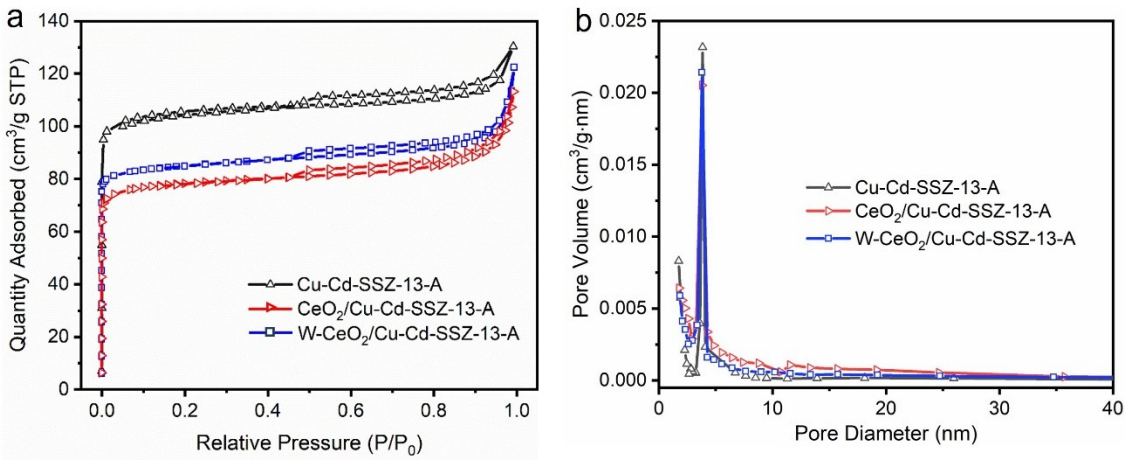

Fig. S6. BET analysis of Cu-Cd-SSZ-13-A, CeO_2/Cu-Cd-SSZ-13-A, W-CeO_2/Cu-Cd-SSZ-13-A (a) N_2 absorption/desorption curve, (b) Aperture distribution curve.

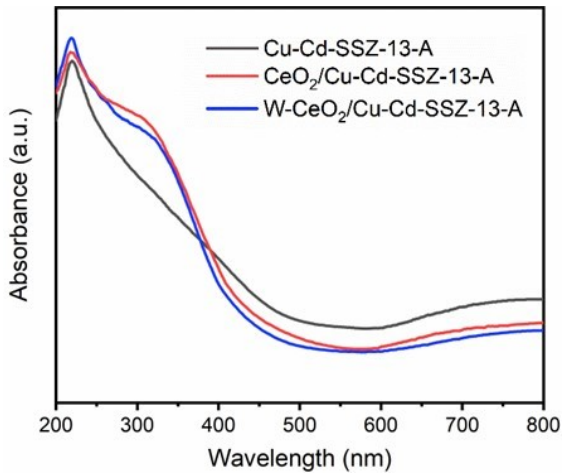

Fig. S7. UV–vis DRS spectra of Cu-Cd-SSZ-13-A, CeO_2/Cu-Cd-SSZ-13-A and W-CeO_2/Cu-Cd-SSZ-13-A.

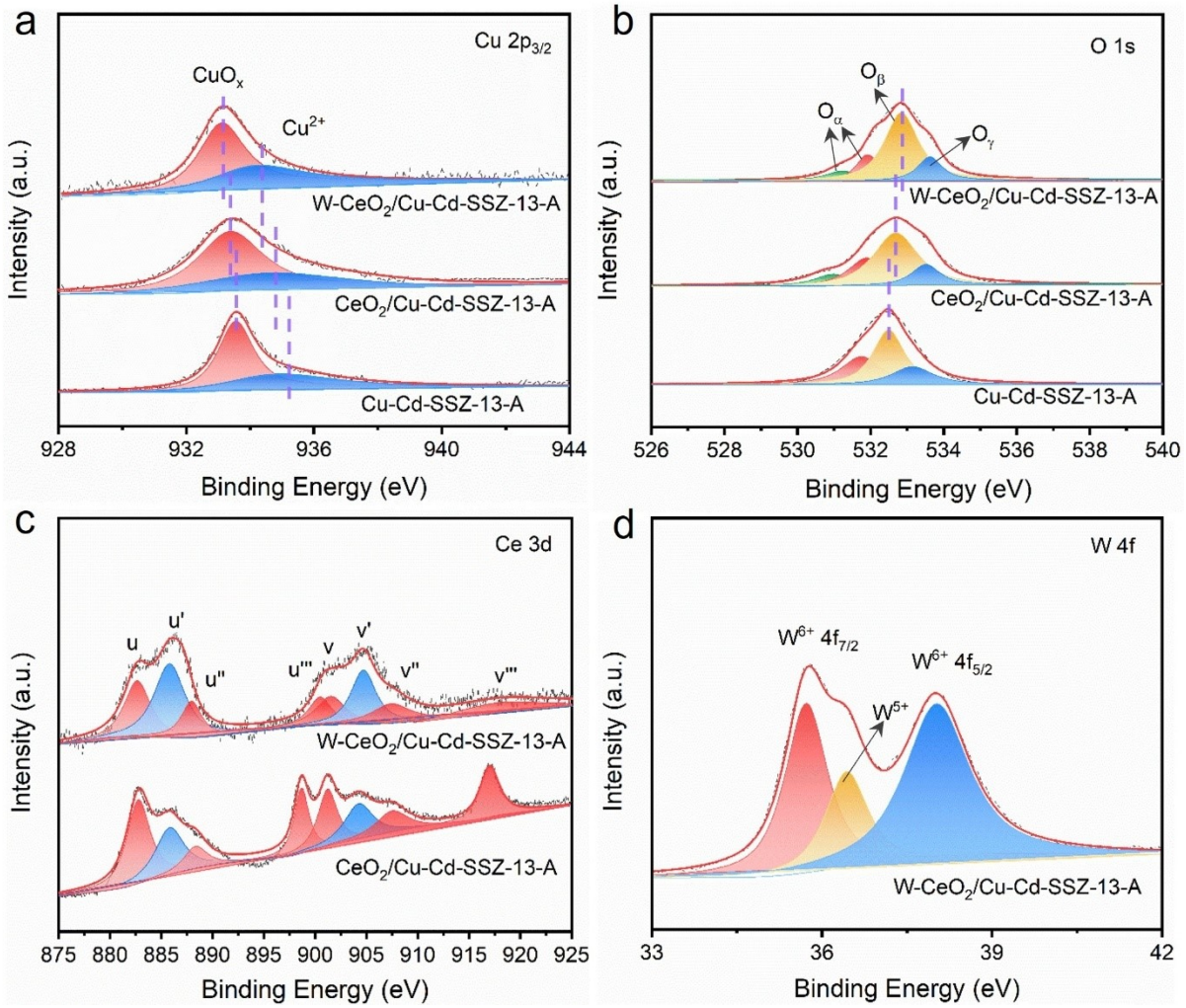

Fig. S8. (a) Cu $2p_{3/2}$, (b) O 1s XPS speactra of Cu-Cd-SSZ-13-A, CeO_2/Cu-Cd-SSZ-13-A and W-CeO_2/Cu-Cd-SSZ-13-A, (c) Ce 3d XPS spectra of CeO_2/Cu-Cd-SSZ-13-A and W-CeO_2/Cu-Cd-SSZ-13-A, (d) W 4f XPS spectra of W-CeO_2/Cu-Cd-SSZ-13-A

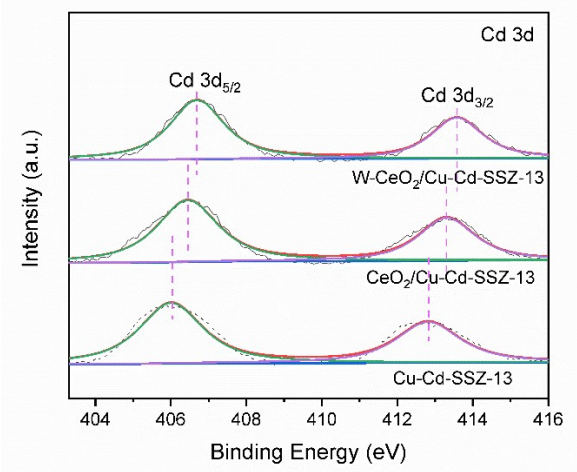

Fig. S9. Cd 3d XPS spectra of Cu-Cd-SSZ-13, CeO_2/Cu-Cd-SSZ-13, and W-CeO_2/Cu-Cd-SSZ-13.

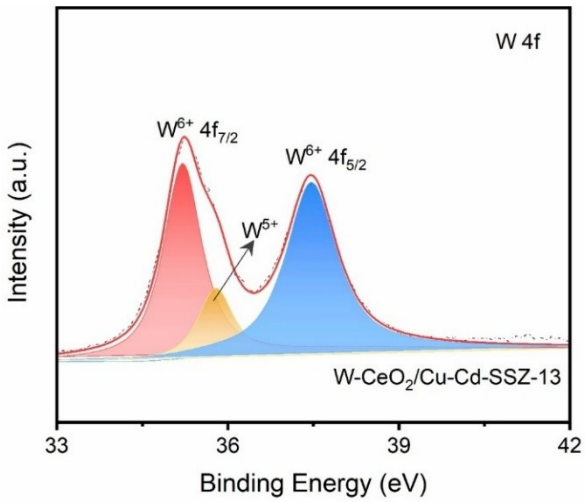

Fig. S10. W 4f XPS spectra of W-CeO_2/Cu-Cd-SSZ-13.

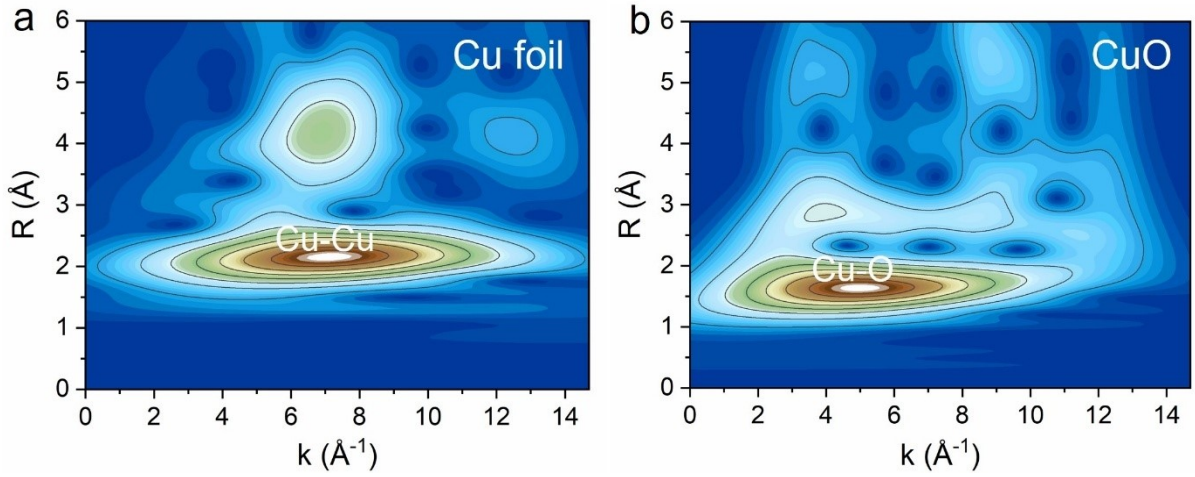

Fig. S11. WT contour plots of (a) Cu foil, (b) CuO.

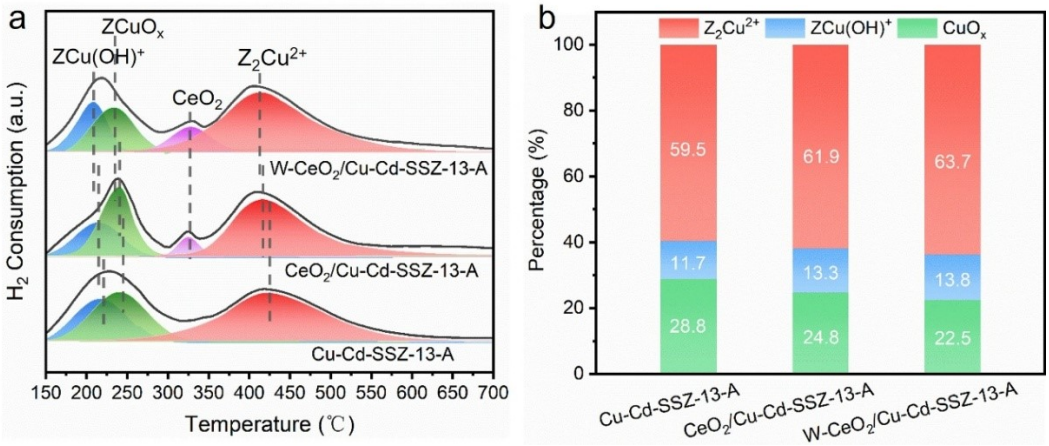

Fig. S12. (a) H_2-TPR profiles, (b) distribution of Cu species for Cu-Cd-SSZ-13-A, CeO_2/Cu-Cd-SSZ-13-A and W-CeO_2/Cu-Cd-SSZ-13-A.

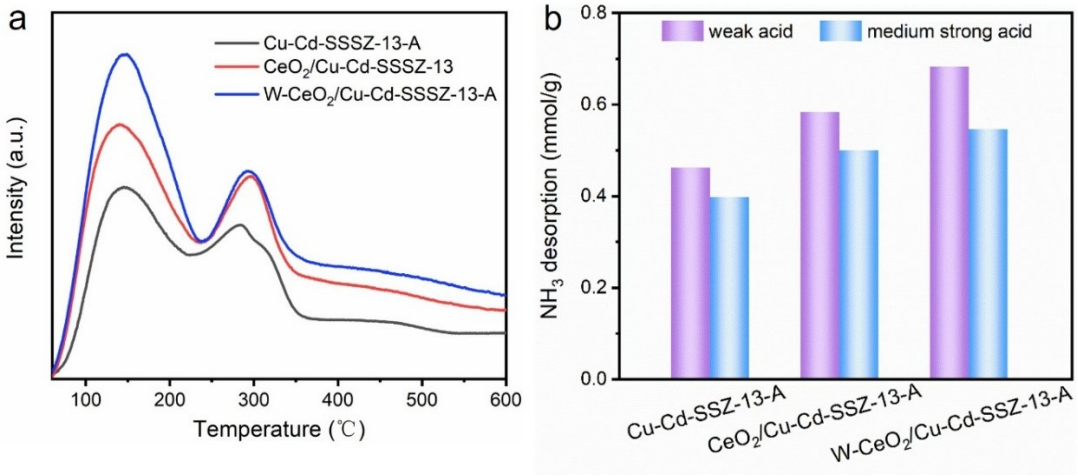

Fig. S13. (a) NH_3-TPD curves, (b) NH_3 desorption amount of Cu-Cd-SSZ-13-A, CeO_2/Cu-Cd-SSZ-13-A and W-CeO_2/Cu-Cd-SSZ-13-A.

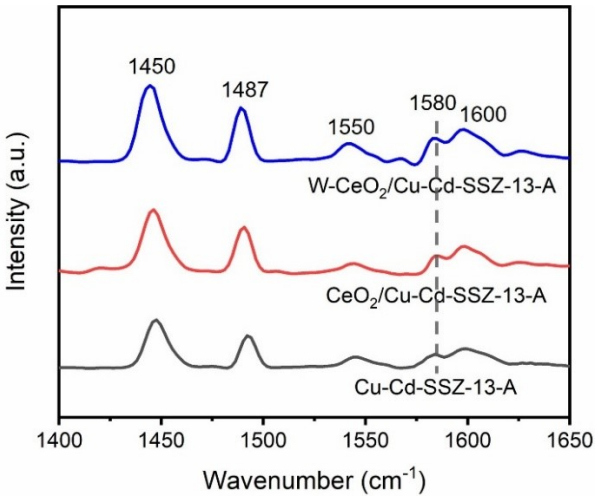

Fig. S14. Pyridine IR spectra of Cu-Cd-SSZ-13-A, CeO_2/Cu-Cd-SSZ-13-A and W-CeO_2/Cu-Cd-SSZ-13-A at 150 ℃.

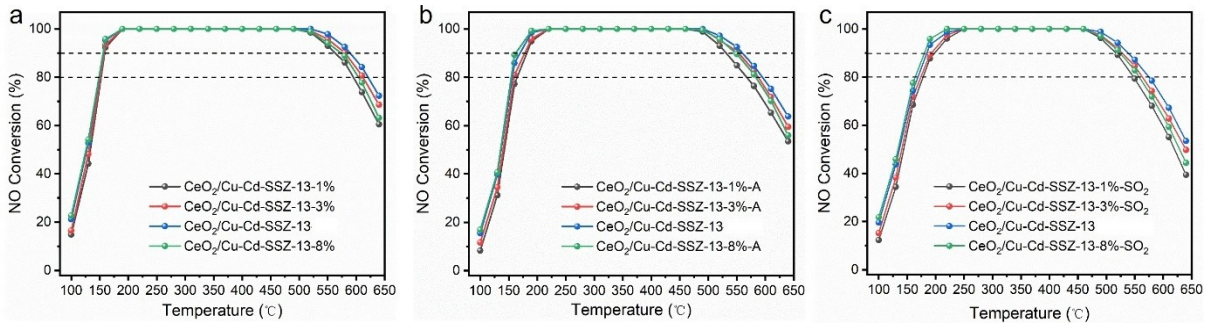

Fig. S15. NO conversion of CeO_2/Cu-Cd-SSZ-13 with different CeO_2 loading (a) before and (b) after high-temperature hydrothermal aging, (c) SO_2 resistance.

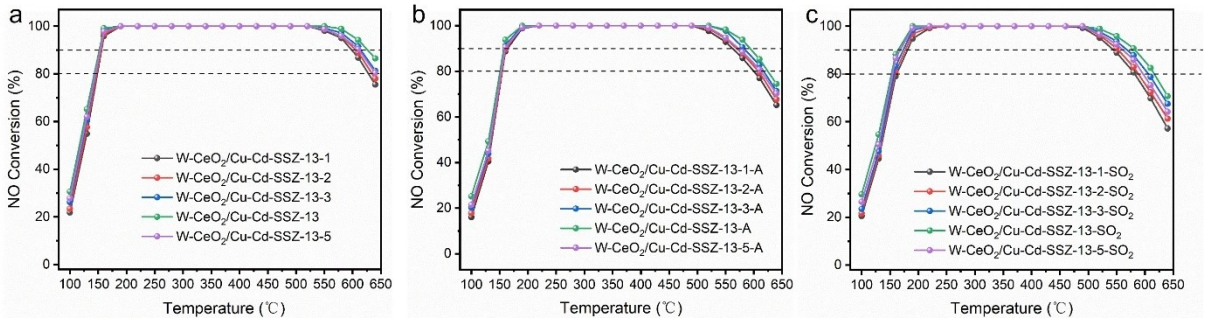

Fig. S16. NO conversion of W-CeO_2/Cu-Cd-SSZ-13 with different W loading (a) before and (b) after high-temperature hydrothermal aging, (c) SO_2 resistance.

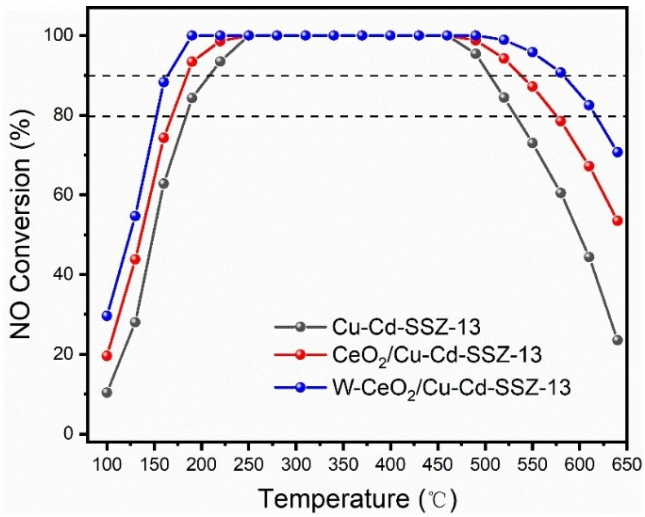

Fig. S17. SO_2 resistance of different samples under GHSV of 60,000 h^{-1}.

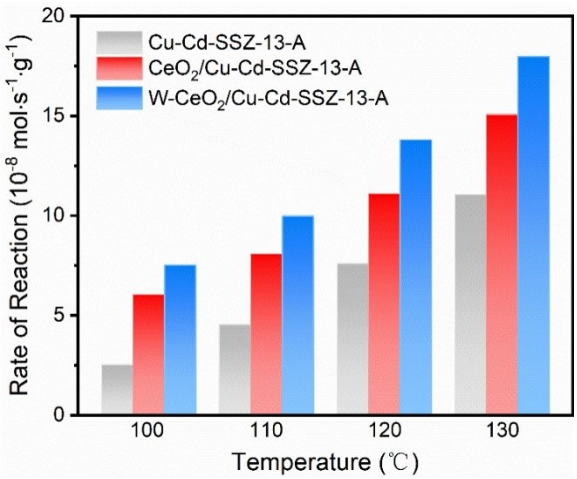

Fig. S18. The NO reduction reaction rate normalized to the mass of different catalysts after hydrothermal aging process.

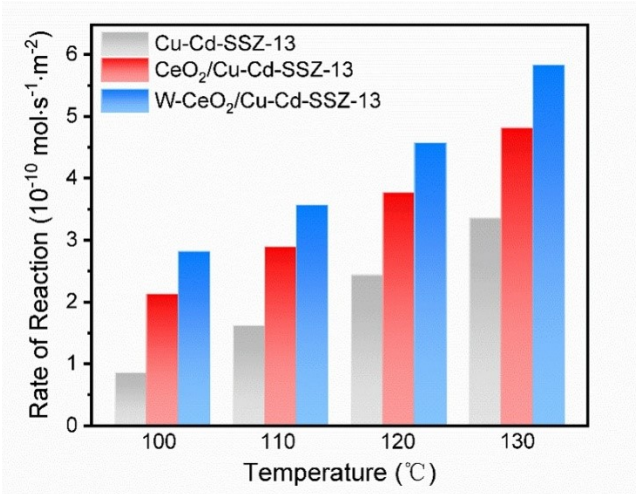

Fig. S19. The NO reduction reaction rate normalized to the specific surface area of different catalysts.

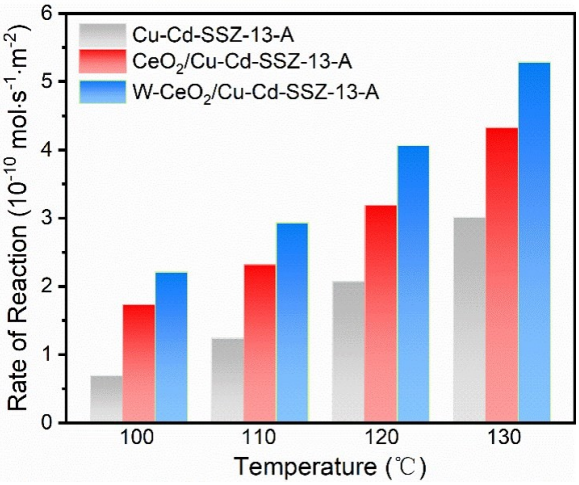

Fig. S20. The NO reduction reaction rate normalized to the specific surface area of different catalysts after hydrothermal aging.

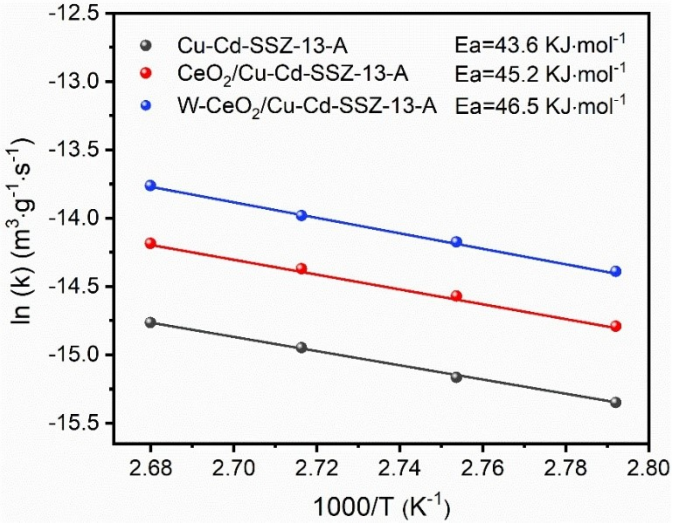

Fig. S21. Arrhenius plots of different catalysts after hydrothermal aging.

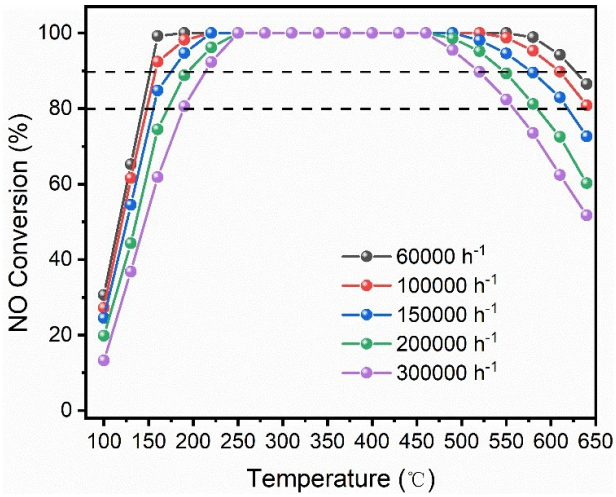

Fig. S22. NO conversion of W-CeO_2/Cu-Cd-SSZ-13 under different GHSV.

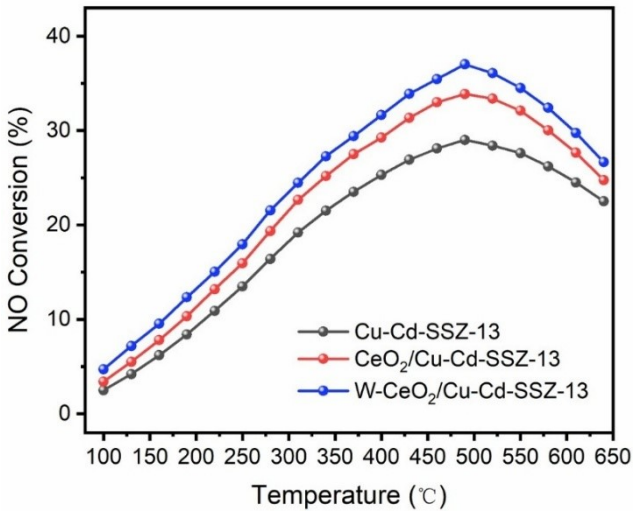

Fig. S23. The NO oxidation activity of different samples under GHSV of 60,000 h^{-1}.

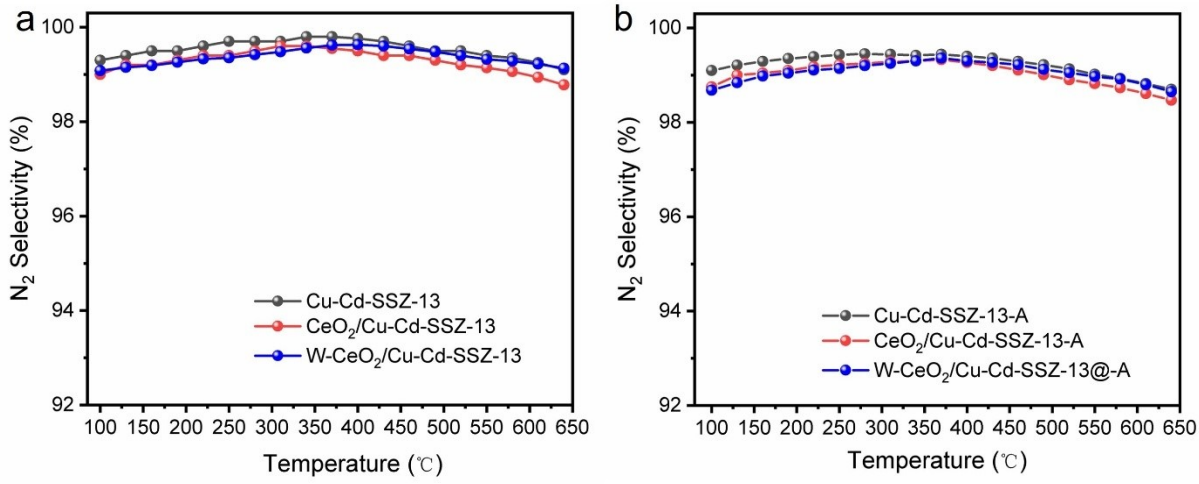

Fig. S24. The N_2 selectivity of different samples (a) before and (b) after high-temperature hydrothermal ageing under GHSV of 60,000 h^{-1}.

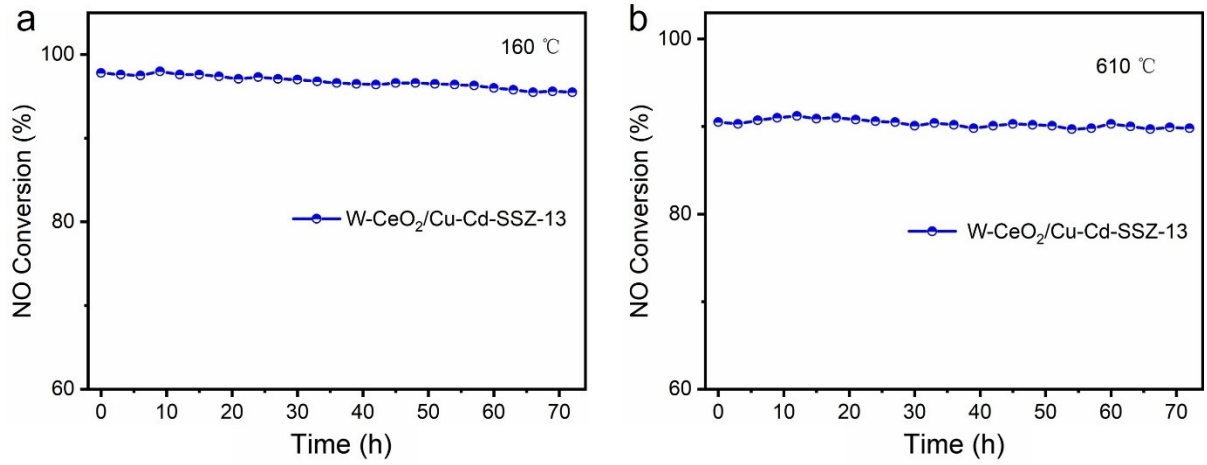

Fig. S25. The NH_3-SCR stability test of W-CeO_2/Cu-Cd-SSZ-13 at 160 and 610℃.

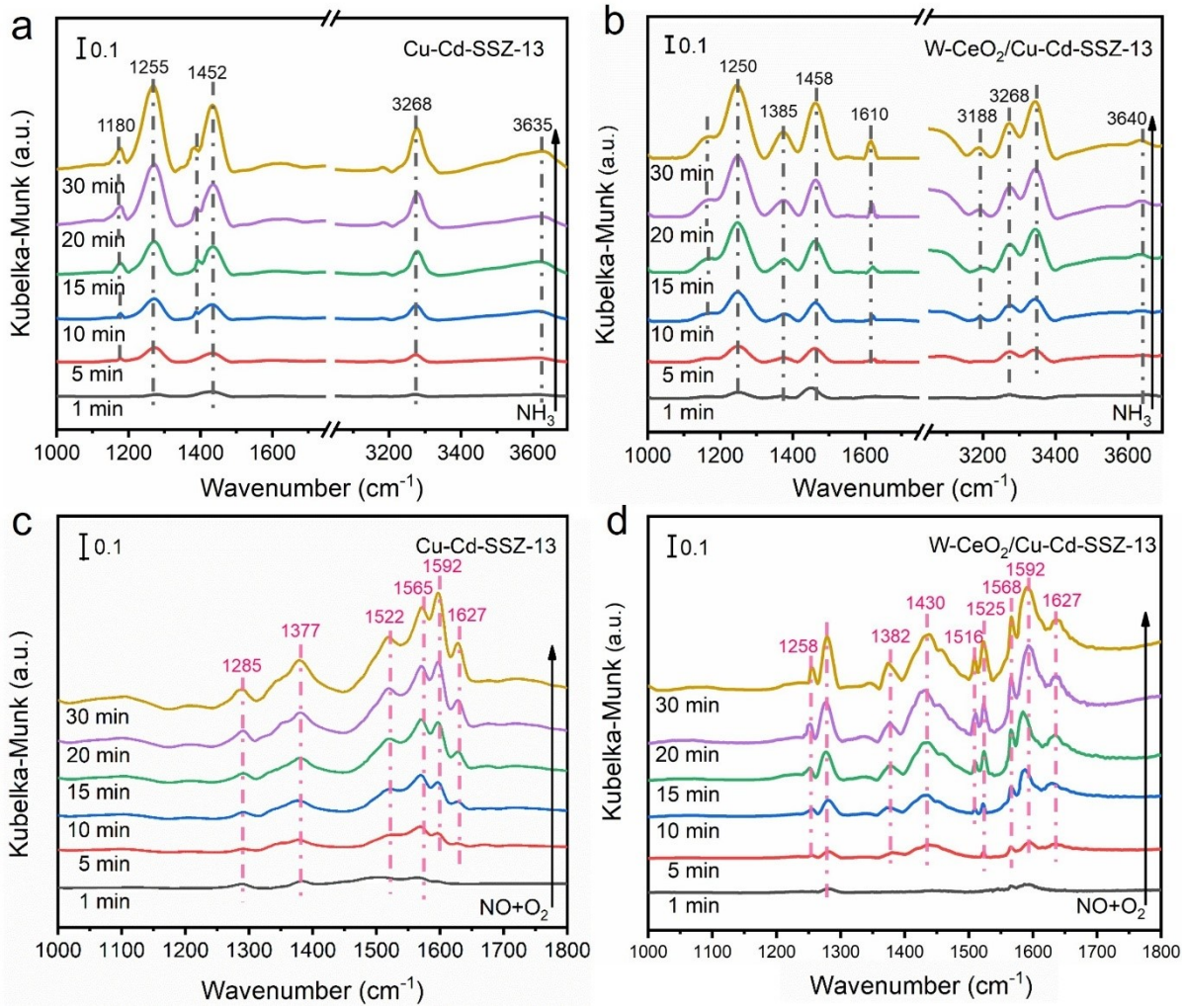

Fig. S26. The *In situ* DRIFTS spectra of NH_3 adsorption over (a) Cu-Cd-SSZ-13 and (b) W-CeO_2/Cu-Cd-SSZ-13, and NO + O_2 co-adsorption over (c) Cu-Cd-SSZ-13 and (d) W-CeO_2/Cu-Cd-SSZ-13 at 130 °C.

Table S1 The ICP element content data of catalysts.

Catalysts	Si/Al	Cu wt%	Cd wt%	Ce wt%	W wt%
Cu-Cd-SSZ-13	7.58	4.56	2.24	/	/
CeO_2/Cu-Cd-SSZ-13	7.55	4.53	2.22	4.37	/
W-CeO_2/Cu-Cd-SSZ-13	7.55	4.53	2.21	4.35	0.58

Table S2 BET analysis of different catalysts before and after hydrothermal aging.

Catalysts	S_{BET} ($m^2 \cdot g^{-1}$)	V_{total} ($cm^3 \cdot g^{-1}$)	V_{micro} ($cm^3 \cdot g^{-1}$)
Cu-Cd-SSZ-13	454.68	0.24	0.23
Cu-Cd-SSZ-13-A	366.65	0.19	0.16
CeO_2/Cu-Cd-SSZ-13	397.87	0.22	0.20
CeO_2/Cu-Cd-SSZ-13-A	339.83	0.16	0.13
W-CeO_2/Cu-Cd-SSZ-13	407.72	0.23	0.21
W-CeO_2/Cu-Cd-SSZ-13-A	348.22	0.18	0.14

Table S3 Surface atomic Cu concentrations of different catalysts before and after hydrothermal aging determined by XPS.

Catalysts	Cu^{2+}/(CuO+Cu^{2+}）(%)	CuO/(CuO+Cu^{2+}）(%)
Cu-Cd-SSZ-13	40.47	59.53
Cu-Cd-SSZ-13-A	35.56	64.44
CeO_2/Cu-Cd-SSZ-13	43.14	58.86
CeO_2/Cu-Cd-SSZ-13-A	38.47	61.53
W-CeO_2/Cu-Cd-SSZ-13	44.82	55.19
W-CeO_2/Cu-Cd-SSZ-13-A	41.97	59.03

Table S4 Surface atomic oxygen concentrations of different catalysts before and after hydrothermal aging determined by XPS.

Catalysts	$O_\alpha/(O_\alpha+O_\beta+O_\gamma)$ (%)	$O_\beta/(O_\alpha+O_\beta+O_\gamma)$ (%)	$O_\gamma/(O_\alpha+O_\beta+O_\gamma)$ (%)
Cu-Cd-SSZ-13	27.22	64.46	18.32
Cu-Cd-SSZ-13-A	30.42	49.54	20.04
CeO_2/Cu-Cd-SSZ-13	25.35	59.28	15.37
CeO_2/Cu-Cd-SSZ-13-A	26.73	56.15	17.12
W-CeO_2/Cu-Cd-SSZ-13	24.24	62.51	13.25
W-CeO_2/Cu-Cd-SSZ-13-A	24.54	59.49	15.97

Table S5 Surface atomic Ce concentrations of catalysts before and after hydrothermal aging determined by XPS.

Catalysts	$Ce^{3+}/(Ce^{3+}+Ce^{4+})$ (%)	$Ce^{4+}/(Ce^{3+}+Ce^{4+})$ (%)
CeO_2/Cu-Cd-SSZ-13	23.87	76.13
CeO_2/Cu-Cd-SSZ-13-A	28.39	71.61
W-CeO_2/Cu-Cd-SSZ-13	28.71	71.29
W-CeO_2/Cu-Cd-SSZ-13-A	40.16	59.84